

1 Estimating the Material Properties of Heel Pad Sub-layers
2 Using Inverse Finite Element Analysis

3 Nafiseh Ahanchian^{a,*}, Christopher J. Nester^a, David Howard^b, Lei Ren^c, Daniel Parker^a

4 ^a School of Health Sciences, University of Salford, Salford, UK

5 ^b School of Computing, Science & Engineering, University of Salford, Salford, UK

6 ^c School of Mechanical, Aerospace and Civil Engineering, University of Manchester, UK

7
8 **Accepted Original Article**

9 We declare that all authors were fully involved in the study and preparation of the manuscript and that
10 the material within has not been and will not be submitted for publication elsewhere.

11 **Word count** (Abstract to Discussion): 4900 words

12
13
14 ***Corresponding Author:** Nafiseh Ahanchian

15 Phone number: +44 (0) 7828675154

16 Email: nahanchian@yahoo.co.uk; N.Ahanchian@salford.ac.uk

24 **Abstract**

25 Detailed information about the biomechanical behaviour of plantar heel pad tissue contributes to our
26 understanding of load transfer when the foot impacts the ground. The objective of this work was to
27 obtain the hyperelastic and viscoelastic material properties of heel pad sub-layers (skin, micro-
28 chamber and macro-chamber layers) *in-vivo*.

29 An anatomically detailed 3D Finite Element model of the human heel was used to derive the sub-layer
30 material properties. A combined ultrasound imaging and motorised platform system was used to
31 compress heel pad and to create input data for the Finite Element model. The force-strain responses of
32 the heel pad and its sub-layers under slow compression (5mm/s) and rapid loading-hold-unloading
33 cycles (225mm/s), were measured and hyperelastic and viscoelastic properties of the three heel pad
34 sub-layers were estimated by the model.

35 The loaded (under ~315N) thickness of the heel pad was measured from MR images and used for
36 hyperelastic model validation. The capability of the model to predict peak plantar pressure was used
37 for further validation. Experimental responses of the heel pad under different dynamic loading
38 scenarios (loading-hold-unloading cycles at 141mm/s and sinusoidal loading with maximum velocity
39 of 300mm/s) were used to validate the viscoelastic model.

40 Good agreement was achieved between the predicted and experimental results for both hyperelastic
41 (<6.4% unloaded thickness, 4.4% maximum peak plantar pressure) and viscoelastic (Root Mean
42 Square errors for loading and unloading periods <14.7%, 5.8% maximum force) simulations. This
43 paper provides the first definition of material properties for heel pad sub-layers by using *in-vivo*
44 experimental force-strain data and an anatomically detailed 3D Finite Element model of the heel.

45 **1. Introduction**

46 The behaviour of the plantar heel pad has been the topic of considerable research because it forms a
47 critical interface with the supporting surface. It is affected by aging and disease and is the site of pain
48 [1, 2, 3]. Study of heel pad behaviour has been achieved through experimental [4, 5, 6] and numerical
49 methods, particularly Finite Element Analysis (FEA) [7, 8, 9]. The latter provides data such as the

50 distribution of internal tissue stress that cannot be experimentally measured. However, for FEA
51 models to prove effective they should be based on geometric and material properties that ensure the
52 model behaviour is sufficiently close to *in-vivo* heel pad behaviour, as seen during human gait.

53 In most Finite Element (FE) models, hyperelastic rather than viscoelastic material models were used
54 to simulate nonlinear behavior of the heel pad [7, 8, 9, 10]. Results from these studies were limited to
55 static or fixed loading rates due to the absence of a dynamic *in-vivo* system that allows compression of
56 plantar tissues at various high speeds, whilst also providing the data required for estimation of
57 viscoelastic parameters and validation.

58 In addition, the heel pad is typically modelled as a homogeneous single-layer material rather than an
59 *in-vivo* tri-layer biological structure (macro, micro and skin layers) [7, 10, 11]. In a few cases, the heel
60 pad was modelled as a dual-layer composite structure (fat and skin), but this ignores the different
61 behaviours and interactions between micro and macro layers [8, 9, 12]. This may compromise the
62 ability of FEA to predict internal stresses.

63 A further issue with some of the models reported thus far is that experimental data were obtained *ex-*
64 *vivo* [12, 13, 14, 15]. Tissue dissection disrupts the normal *in-vivo* tissue constraints and the effects of
65 time and loss of vascular supply are not fully understood [16]. Clearly, *in-vivo* methods at appropriate
66 loading rates are preferred over *ex-vivo* approaches.

67 In summary, most of heel pad models are limited by excluding viscoelastic effects and/or using less
68 than three layers. Moreover, some approaches to validation may not test models with sufficient rigour.
69 Hence, the objective of this work was to estimate hyperelastic and viscoelastic material properties of
70 ‘macro-chamber’, ‘micro-chamber’ and ‘skin’ layers using inverse FEA and *in-vivo* experimental
71 data.

72 **2. Methods**

73 **2.1 Finite Element Model**

74 An anatomically detailed model of the right heel of a healthy female volunteer (34 years old, height
75 164cm, weight 63kg, shoe size 5UK) was constructed based on unloaded MRI images. MRI data were
76 T1 weighted with a flip angle of 25, taken in coronal view using 3D fast field echo (Philips 1.5T
77 Acheiva), with pixel size=0.29mm×0.29mm (2.4% resolution), and slice intervals=1.25mm. The
78 images were segmented to identify the plantar fascia, muscle tissue, macro-chamber, micro-chamber
79 and skin layers and create corresponding 3D surface geometries using ScanIP v3.1 (Simpleware Ltd,
80 Exeter, UK). Different segmentation algorithms including thresholding, confidence connected region-
81 growing, floodfill and paint were used for identifying the corresponding tissues. 3D surface
82 geometries were imported into SolidWorks 2010 (Dassault Systemes, USA) to generate 3D solid
83 geometries and the complete assembly. Since MRI slices were out of the plane of boundaries between
84 soft tissue layers, the effect on structural modelling will be minimal. Also, the 0.29mm between slices
85 is a small percentage of the anterior/posterior length of the structured modelled. A full description of
86 the development of the heel region structures can be found elsewhere [17].

87 To reduce the computation time only a portion of the foot was modelled. Planes at 92.5mm from the
88 back and 45mm from the bottom of the heel were chosen to be flat face boundaries of the model. The
89 solid model was meshed with 11,504 hexahedral elements (type C3D8R) using ABAQUS v6.10
90 (Dessault Systemes, USA).The number of elements was obtained by performing a mesh convergence
91 study. The selected mesh density was based on the change in the peak force for a subsequent doubling
92 of mesh density being less than 3%. The meshed model was exported to Ls-Dyna v2.2 (Livermore
93 Software Technology Corporation, Livermore, USA) for inverse FEA. Effects of stiff tissues (foot
94 bones and Achilles tendon) on the biomechanical behaviour of the heel pad were simulated by
95 applying zero-displacement constraints to all nodes forming the soft tissue-stiff tissue interface. The
96 Achilles was modelled as stiff since under tension it will be far stiffer than the fat pad and far from it
97 too, acting as a rigid attachment to the heel bone which is thereafter attached to the heel pad. All
98 nodes at the superior and anterior boundaries (flat faces) of the model were fully constrained. The
99 model was tilted by 17° to replicate the position of the foot during subsequent experiments performed
100 with a Soft Tissue Response Imaging Device (STRIDE) (Figure 1) [18]. In Ls-Dyna the flat

101 indentation plate of the STRIDE was modelled as a rigid structure (Figure 1). Tied contact was
102 defined between the parts of the heel model and frictionless surface-to-surface contact was defined
103 between the indentation plate and heel skin.

104 The macro-chamber, micro-chamber and skin were modelled as nonlinear viscoelastic materials
105 (Figure 1). The first-order Ogden model was used to represent the hyperelastic behaviour of heel pad
106 tissues as done previously [7, 8, 9]. The corresponding material properties appear in the strain energy
107 function as follows

$$108 \quad W = \frac{\mu}{\alpha} (\lambda_1^\alpha + \lambda_2^\alpha + \lambda_3^\alpha - 3) \quad (1)$$

109 where λ_{1-3} are the principal stretches in the x, y and z directions respectively, μ is the shear modulus,
110 and α is the deviatoric exponent (μ and α being the hyperelastic material parameters). Viscoelastic
111 tissue behaviour was modelled using one generalized Maxwell element for the viscoelastic overstress
112 in the Ogden model. The Maxwell viscoelastic element consists of a linear spring with stiffness G_1
113 and a linear damper with viscosity ν_1 in series. The relaxation time (a measure of the time taken for
114 the stress to relax) for the Maxwell unit is $\tau_1 = \nu_1 / G_1$. Its inverse is the decay constant $\beta_1 = 1 / \tau_1$. The
115 stiffness G_1 (the shear relaxation modulus) and decay constant β_1 are the viscoelastic material
116 parameters of the model in Ls-Dyna. The corresponding material properties appear in the relaxation
117 function, $G(t)$, written as a first-order Prony series, representing the combined hyperelastic and
118 viscoelastic model as follows

$$119 \quad G(t) = G_\infty + G_1 e^{-\beta_1 t} \quad (2)$$

120 where G_∞ is the long term shear modulus (Figure 1).

121

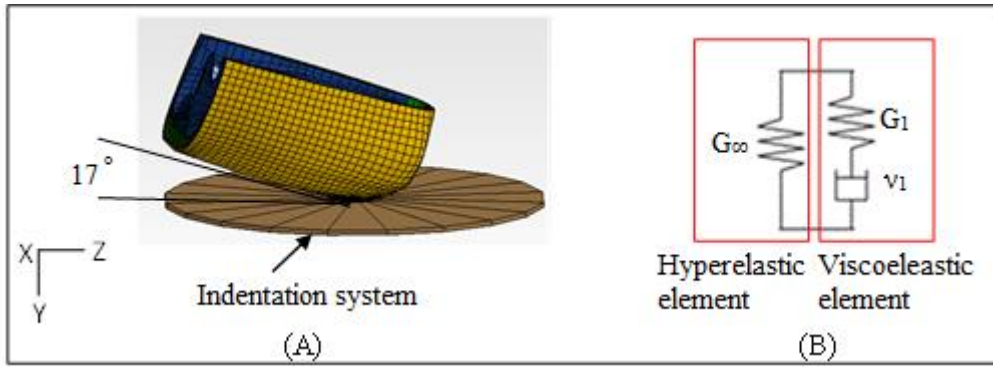


Figure 1. (A) The complete meshed model of the heel region; (B) The behaviour of the tissues making up the three layers was modelled using a combination of an Ogden hyperelastic model and a Maxwell element

The focus of the reported work is to identify the properties of and model the heel pad. However, the surrounding tissues that constrain the heel pad must also be modelled adequately enough to provide realistic boundary conditions. Therefore, to simplify the FE model, the plantar fascia and muscle tissues were modelled as linear elastic materials. However, the literature contains limited reports concerning the material properties of muscle tissues and plantar fascia and, in most other FE studies, the foot muscles have been merged with the heel pad tissue and assigned the same material properties [19, 20, 21]. Moreover, the plantar fascia has previously been modelled with tension-only truss elements with Young's modulus determined from tensile tests [19, 20, 22]. Since there is poor agreement between studies, a series of parametric studies was conducted to assess the sensitivity of the FEA results to the material properties used for the plantar fascia and muscle tissue. Different material properties, derived from published data [21, 22, 23, 24, 25], were assigned to the plantar fascia and muscle tissue and this revealed only a small effect on the force-strain behaviour of the heel pad (Root Mean Square (RMS) error <1.5% and <0.67% max force for the plantar fascia and muscle tissue respectively). The initial material properties derived from published literature were therefore used to start the FEA (Table 1).

Table 1
Initial material properties of each component in the FE model

	Material model	Material properties	Poisson's ratio	Density (g/mm ³)	References
Muscle tissue	Linear elastic	E=1.08MPa	0.49	1×10 ⁻³	[22]

Plantar fascia	Linear elastic	$E=350\text{MPa}$	0.40	1×10^{-3}	[19, 22]
Heel pad sub-layers	Hyperelastic	$\mu=0.016\text{MPa}$, $\alpha=6.82$	0.4999	1×10^{-3}	[7]
	Viscoelastic	$G_1=0.389\text{MPa}$, $\beta_1=1000\text{s}^{-1}$			[26]
Indentation system	Rigid	$E=2.07\times 10^5\text{MPa}$	0.3	7.83×10^{-3}	

143

144 2.2 Experimental Acquisition of Force and Tissue Displacement Data

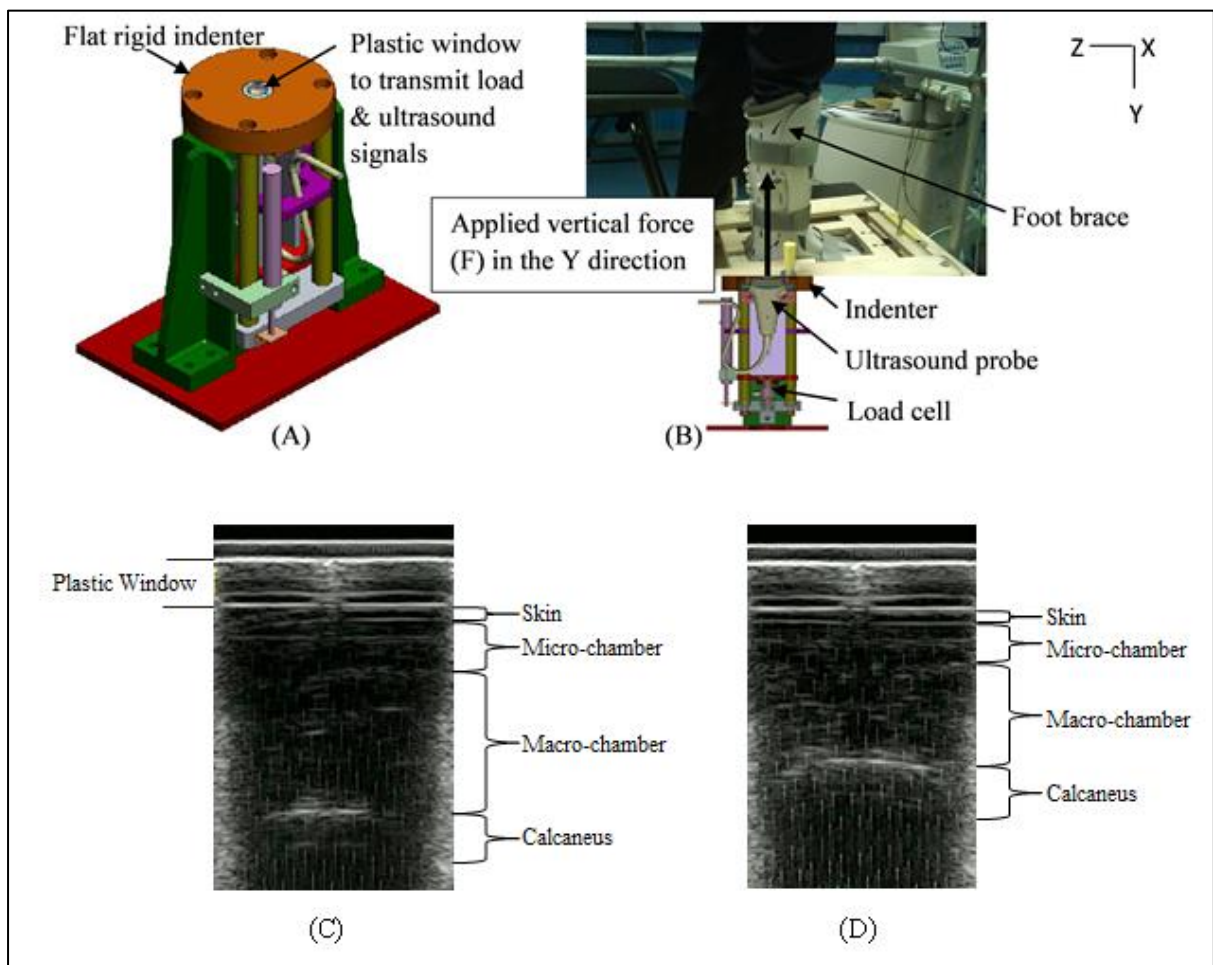
145 The aim of this stage was to perform a series of slow and rapid compression tests on the same heel
 146 used to generate the geometric model and obtain the force-strain responses of the heel pad and its sub-
 147 layers. Ethical approval was granted by the University of Salford ethical committee.

148 STRIDE applies controlled vertical compression cycles of various speeds and load profiles to the heel
 149 pad *in-vivo*. It simultaneously uses an ultrasound system with a 5.5MHz probe in B-Mode and capture
 150 frequency of 201Hz (MyLab 70, Esaote, Italy) with a measurement accuracy of 1.75% ($\pm 0.7\text{mm}$) to
 151 track changes in the heel pad and the boundaries between its sublayers during loading/unloading.
 152 STRIDE uniformly compresses the heel using a 150mm diameter flat rigid steel plate. A 20mm
 153 diameter circular plastic window at the centre of the plate allows imaging of the tissue. Example of
 154 ultrasound images (for the unloaded and loaded heel pad) is shown in Figures 2. The boundary of the
 155 calcaneus can be seen as a white, thick arc at the lower part of the ultrasound images. The interface
 156 between the macro-chamber and micro-chamber layers is the indistinct thick white layer in the middle
 157 of the ultrasound images. However, by adjusting the brightness and contrast of the images, this
 158 boundary becomes much clearer at the expense of the other features. The boundaries of the skin layer
 159 are thin white bands, one adjacent to the plastic window and the other forming the interface with the
 160 micro-chamber layer. As can be seen, static ultrasound images are difficult to interpret. However, the
 161 ultrasound videos of the indentation process clearly show the moving boundaries and then the
 162 boundaries in the corresponding static images can be identified by cross-referencing with the videos
 163 (Video 1). The ultrasound images were used to measure the unloaded and loaded thickness (UT and
 164 LT) of the heel pad, macro-chamber and micro-chamber layers in the vertical Y direction (i.e.

165 perpendicular to the flat indenter surface in Figure 2). The engineering strains of the three tissue
 166 layers were then calculated as follows:

167
$$\varepsilon = \frac{UT-LT}{UT} \quad (3)$$

168 These measurements were taken under the calcaneus tuberosity above the plastic window (Figure 2).
 169 The vertical compression force in the Y direction, F in Figure 2, applied to the tissue above the
 170 window is measured independently of the total load applied to heel area using a miniature load cell
 171 (500lb Precision, 3000Hz, TC34, Amber Instrument, UK) with linearity of 0.02% (4.45N). The load
 172 recorded under the heel pad by the miniature load cell versus strains of heel pad, macro-chamber and
 173 micro-chamber was used as input to the FEA. All tests were done while the subject was standing and
 174 the calcaneus tuberosity located above the centre of the window. The foot was in a foot brace (Aircast
 175 boot) which allowed vertical compression of the heel without lifting of the foot (Figure 2).



176

177 Figure 2. Soft Tissue Response Imaging Device (STRIDE) and ultrasound images for the frontal
178 view at the location of calcaneus tuberosity: (A) Isometric view of STRIDE; (B)
179 Cross-section and foot brace arrangement; (C) Unloaded heel pad; (D) Loaded heel
180 pad

181 The moving boundaries of the heel pad sub-layers can be seen more clearly in the ultrasound video
182 clip recorded during compressing of the heel pad by STRIDE (Video 1).



183 Ultrasound video of compression tracking.mp4

184 Using STRIDE, slow compression tests at 5mm/s and rapid compression tests at 225mm/s
185 (comparable to the velocity of vertical impact in slow walking) were performed in order to determine
186 the material properties of the heel pad sublayers. For these tests, the indenter followed a truncated
187 triangular waveform consisting of 4 phases: load at constant speed; a 26ms hold period; unload at
188 constant speed; a 26ms hold period. For validation of the viscoelastic FE model, another two different
189 loading cycles were applied: (1) load/unload at a constant speed of 141mm/s (with 26ms hold), and
190 (2) sinusoidal loading-unloading cycles with a maximum speed of 300mm/s. These achieved
191 compression of up to 36.5% (5.7mm) the unloaded thickness of the heel pad. The compression tests
192 were repeated for five iterations with 1-minute rest between each trial to allow for tissue recovery.
193 The unloaded thickness of the heel pad sub-layers was measured from the first available ultrasound
194 image i.e. when the indenter first touched the plantar tissue.
195 The force-strain responses of the heel pad and its sub-layers indicated that their behaviours are
196 nonlinear with an initial low stiffness region, followed by increasing stiffness. The results showed that
197 the macro-chamber, micro-chamber and skin layers formed 76.4, 14.7, and 8.9% of the unloaded heel
198 pad thickness respectively. Test results showed that the resistance of the heel pad is increased by
199 increasing loading velocity. During slow compression (5mm/s), an average load of ~73N was required
200 to obtain a 36.5% strain of the heel pad, whereas ~96N and ~114N were required at constant
201 velocities of 141 and 225mm/s. The increase in loading velocity resulted in an increase in Energy
202 Dissipation Ratio (EDR). For compression at 141mm/s, EDR was 63.3%, whereas it was 76.1% at

203 225mm/s. Under sinusoidal loading EDR was measured as 78% that is close to results for impact and
204 ballistic pendulum tests performed on healthy adults (79-90%) [27].

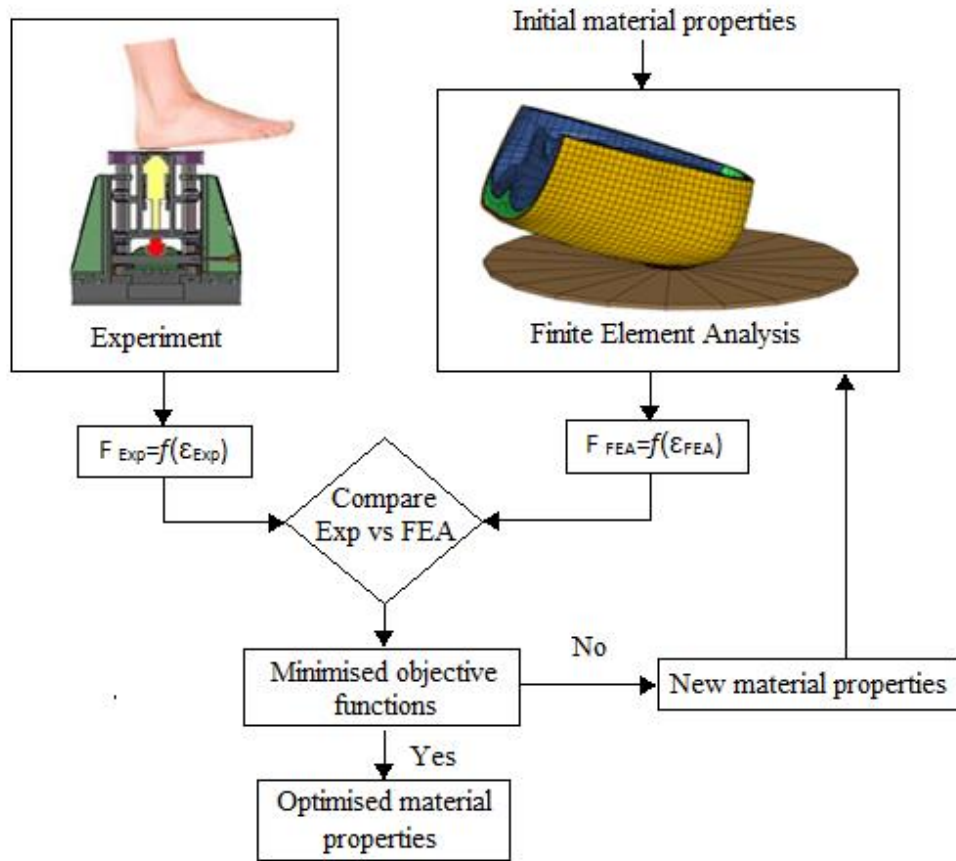
205 **2.3 Inverse Finite Element Analysis**

206 The inverse FEA procedure was broken into multiple stages (associated with the different tissue
207 layers) as shown in Figure 4. This procedure was used twice: firstly to estimate the hyperelastic
208 parameters and then to estimate the viscoelastic parameters. In this way, at each stage only two
209 material properties had to be found, which was done using the manual search technique summarised
210 in Figure 3. The latter will be explained first before describing the multiple stages associated with the
211 different tissue layers.

212 The force-strain responses of the heel pad and its sublayers (Figure 6), obtained from the physical
213 tests, were used as inputs to the manual searches (the FEA model itself being driven by the
214 corresponding indenter motion profiles). Referring to Figure 3, the comparison between experiment
215 and FEA was based on the RMS force error and the difference between maximum strains (calculated
216 using Excel). The RMS error was calculated as follows:

$$217 \quad RMS\ error = \sqrt{\frac{\sum_{k=1}^n (F_{k\varepsilon} - F'_{k\varepsilon})^2}{n}} \quad (4)$$

218 where $F_{k\varepsilon}$ and $F'_{k\varepsilon}$ are model predicted and experimental forces respectively, and k is the data point
219 index. In each manual search, the magnitudes of the adjustments made to the two material properties
220 (e.g. μ and α), for the current tissue layer, were chosen so that the FEA outputs moved gradually
221 towards the experimental results (RMS error decreasing). When the RMS error passed a minimum
222 and started to increase, the adjustments were halved and their sign changed. In this way, the minimum
223 RMS error was found.

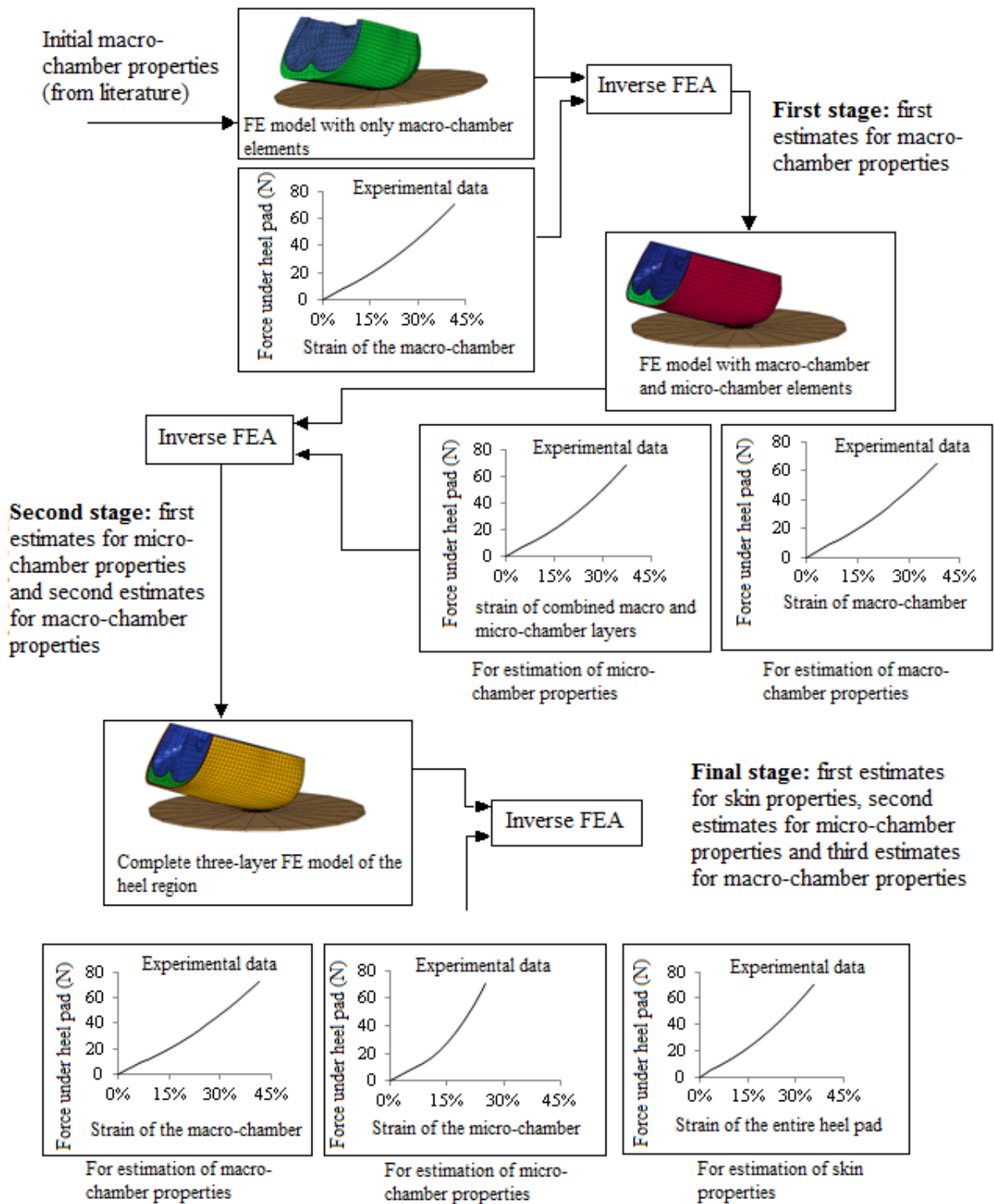


224

225 Figure 3. The manual search procedure; F and ϵ are force and strain respectively. Exp and FEA
 226 refer to experiment and finite element analysis respectively.

227 In the first stage, the macro-chamber layer FE elements (i.e. a one layer model) were used to
 228 determine first estimates of the macro-chamber material properties, which were assigned with initial
 229 values of $\mu=0.016\text{MPa}$ and $\alpha=6.82$ [7]. These properties were then adjusted using the manual search
 230 procedure described above to optimise the fit with the experimental data for the macro-chamber layer.
 231 This process was repeated for 21 iterations until no useful reduction was observed in the RMS error
 232 (i.e. when the change in RMS error between the last two iterations was less than 0.2% of the
 233 maximum force). The parameters determined at this stage were not the final values since they were
 234 obtained in the absence of the constraints applied by the micro-chamber and skin layers *in-vivo*.

235



236

237 Figure 4. Inverse FEA procedure for estimating the material properties of the macro-chamber,
 238 micro-chamber and skin layers

239 In the second stage, the elements representing the micro-chamber were added to the model (i.e. a two-
 240 layer model was created). Micro-chamber properties were adjusted iteratively, starting from properties
 241 derived for the macro-chamber layer, to optimise the fit with the experimental data for the combined

242 macro-micro layers. Additional constraints applied to the macro-chamber layer by the micro-chamber
243 layer inevitably affected the response of the macro-chamber layer. Therefore, the macro-chamber
244 behaviour was reviewed during each iteration alongside the adjustment of micro-chamber material
245 properties, its properties being varied to optimise the fit with the macro-chamber experimental data.
246 The process of adjusting the material parameters of the macro-chamber and micro-chamber layers was
247 repeated for 23 iterations until the objective functions of the macro-chamber layer and two-layer
248 model did not change significantly between iterations (i.e. when $\Delta\text{RMS} < 0.5\%$ of maximum force and
249 $\Delta\text{maximum strain} < 0.05\%$ of maximum strain respectively).

250 In the final stage, the complete model incorporating macro-chamber, micro-chamber and skin layer
251 (i.e. a three-layer model) was used for estimation of the final values of the material parameters of the
252 heel pad sub-layers. Skin properties were adjusted in an iterative procedure, starting from properties
253 derived for the micro-chamber layer, to optimise the fit between predicted results for the complete
254 model and the experimental data for the entire heel pad. Additional constraints applied to the micro
255 and macro-chamber layers by skin layer. Therefore, the properties of micro and macro-chamber layers
256 were again adjusted at each iteration to optimise their individual fits to the experimental data. A total
257 of 71 iterations were required to reach convergence with $\Delta\text{RMS error} < 0.5\%$ of maximum force and
258 $\Delta\text{maximum strain} < 0.02\%$ of maximum strain for determination of hyperelastic material properties.

259 After determination of the hyperelastic material properties, the viscoelastic parameters of the heel pad
260 sub-layers were estimated. In total, 6 viscoelastic parameters had to be estimated, G_1 and β_1 for each
261 of the three heel pad sub-layers. The model was simplified as suggested by Hajjarian & Nakarni, by
262 adopting identical decay constants for the three heel pad sub-layers [28]. A similar procedure to that
263 used to obtain the hyperelastic material properties was followed (Figure 4) by fitting the FE predicted
264 results to the corresponding experimental force-strain data but now using the data from the rapid
265 compression tests (225mm/s). Two RMS force errors (one during loading and another during
266 unloading) were used to assess the quality of the model fit. This process was repeated until the errors

267 did not change significantly with further adjustment (Δ RMS force errors <0.7% of maximum force).

268 Table 2 shows the result of optimisation at each stage for the heel pad sub-layers.

269 **Table 2**

270 Optimisation stages for hyperelastic and viscoelastic models of heel pad sub-layers.

		First Iteration				Final Iteration			
Hyperelastic model		μ (kPa)	α (-)	Difference between maximum strains (%)	RMS (% max force)	μ (kPa)	α (-)	Difference between maximum strains	RMS (% max force)
One layer model		16.45	6.8	-	9.6	41	4.2	-	1.8
Two layer model	Micro-chamber	41	4.2	-	13.3	104	4.7	-	2.6
	Macro-chamber	41	4.2	2.8	8.9	35	4.9	1.4	2.4
Three layer model	Skin	104	4.7	-	9.8	551	3.8	-	2.7
	Micro-chamber	104	4.7	4.5	28.4	100	4	0.3	5.0
	Macro-chamber	35	4.9	3.5	3.7	35	4.2	0.4	2.6
Viscoelastic model		G (MPa)	β ms ⁻¹	RMS error loading (%)	RMS error unloading (%)	G (MPa)	β ms ⁻¹	RMS error loading (%)	RMS error unloading (%)
One layer model		0.39	1	10.1	5.4	0.11	0.08	8.4	5.1
Two layer model	Micro-chamber	0.11	0.08	13.4	6.7	0.46	0.06	10.1	4.3
	Macro-chamber	0.11	0.08	11.9	3.5	0.14	0.06	8.6	2.0
Three layer model	Skin	0.46	0.06	17.8	7.7	0.42	0.12	17.1	1.8
	Micro-chamber	0.46	0.06	13.4	12.7	0.30	0.12	14.4	6.4
	Macro-chamber	0.14	0.06	13.8	4.1	0.24	0.12	14.5	3.1

271 **2.4 Validation**

272 The loaded thickness of the heel pad measured from MRI and the peak plantar pressure under the heel

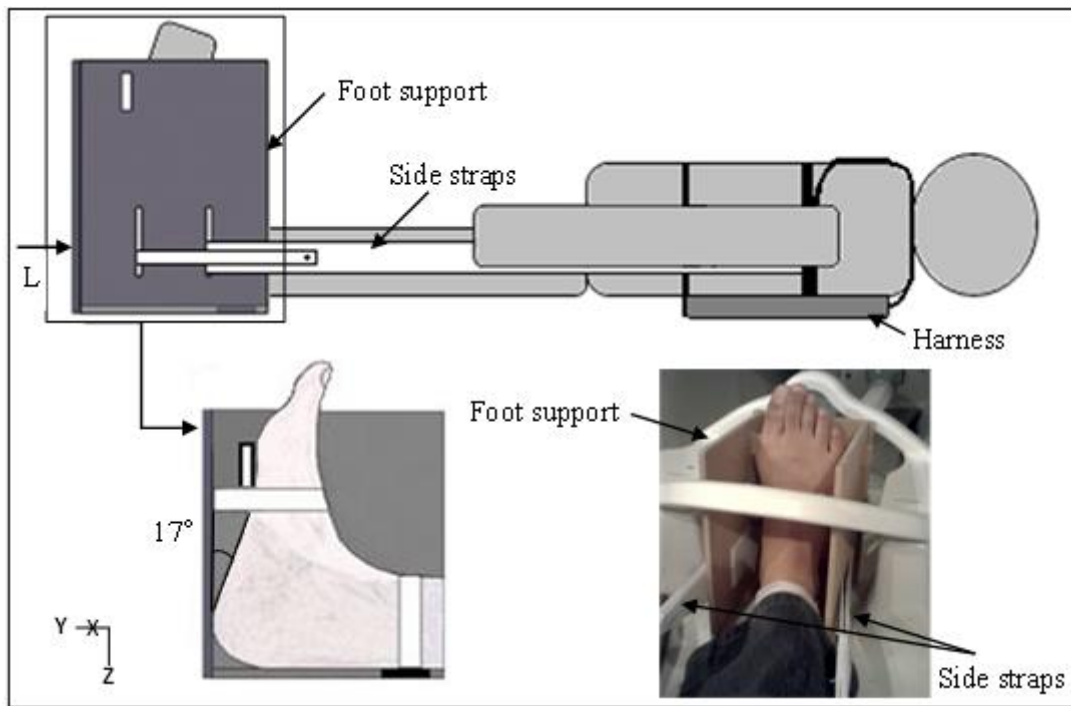
273 were used to validate the hyperelastic FE model. The loaded MRI was taken from the right foot of the

274 subject whose unloaded MRI data was used previously to build the heel pad model. A device was

275 developed to load and vertically compress the heel pad during MRI scanning. The load and

276 compression mimicked the loading in the STRIDE and the FE model. The device comprised of a

277 wooden foot support under the heel (rotated by $\sim 17^\circ$ into dorsi flexion) attached to a harness worn by
278 the subject during scanning. Elastic straps attaching the harness to the footplate were adjusted to
279 create tension and thus compress the heel (Figure 5).



280

281 Figure 5. The heel pad loading device. L = force applied to plantar aspect of heel.

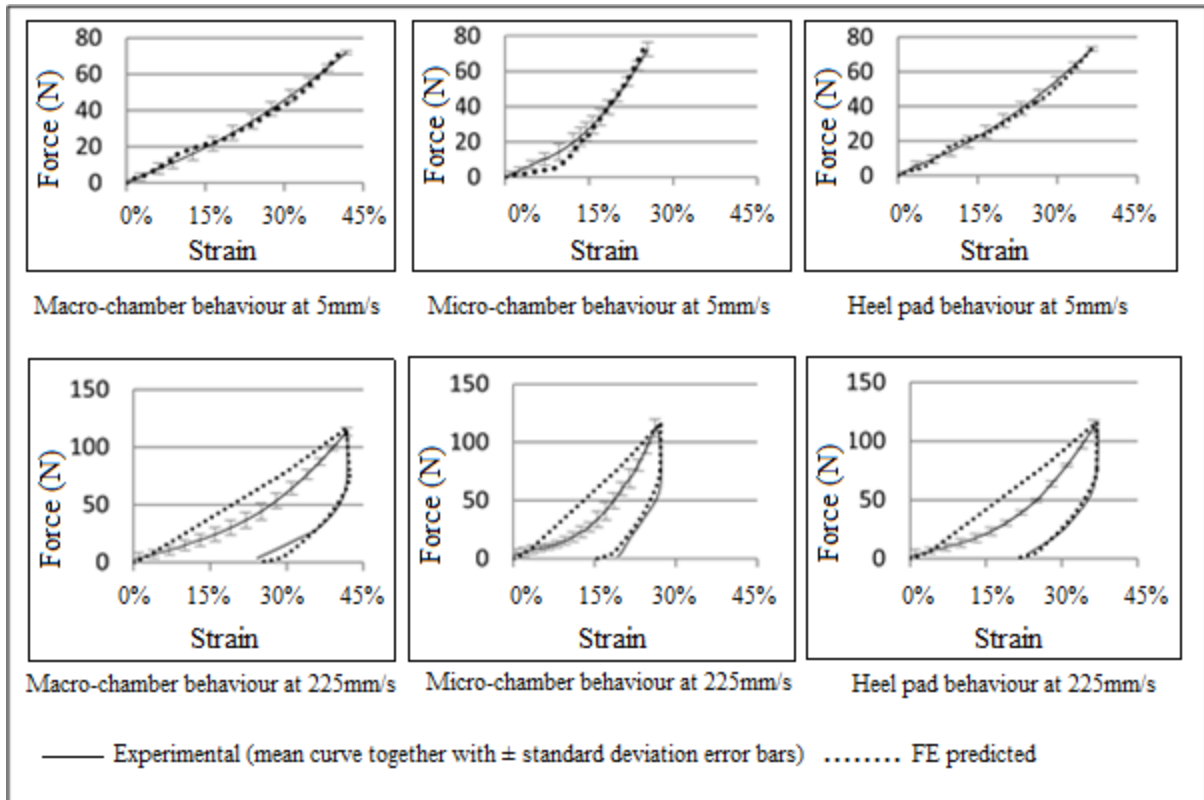
282 The applied load and pressure were measured using a Pedar pressure measurement insole system with
283 a resolution of 2.5-5 kPa (Novel.de, Munich, Germany) before entering the MRI scanner. Some pilot
284 measurements were performed before and after MRI scanning to ensure that using the heel pad
285 loading device provides consistent data out of and during MRI scanning. The force was measured for
286 17 sensors with total area of 3295mm^2 under the heel region. Larger insole than the foot size was
287 selected to ensure that not any load or pressure data of the heel is missed. The T1 MRI scans were
288 taken with 160×160 pixels and spacing of 5.5mm from the heel area in the coronal view. During the
289 MRI scanning, the subject was lying in the supine position. The loaded thickness was measured at the
290 image slice 29mm from the back of the heel, which was closest to the calcaneus tuberosity, and 34mm
291 from the lateral side. To predict the loaded thickness of the heel pad and plantar pressure in the FE
292 model, the indenter and load cell were replaced by a rectangular flat rigid plate.

293 To demonstrate that the viscoelastic FEA model could extrapolate from the results used to find the
294 material properties, different experimental results were used for validation, including results for rapid
295 compression tests at 141mm/s and sinusoidal loading. RMS errors between force-strain responses of
296 the heel pad during loading and unloading periods were used to evaluate the quality of the viscoelastic
297 FE model in reproducing the behaviour of the heel pad at rapid compression tests.

298 **3. Results**

299 Using inverse FEA, hyperelastic and viscoelastic material properties were obtained for the macro-
300 chamber, micro-chamber and skin layers (Figure 6 and Tables 3, 4). In Figure 6 visual inspection of
301 the graphs confirms that the heel pad and its sublayers show nonlinear behaviour under loading. For a
302 36.5% strain of the heel pad under slow compression, macro-chamber and micro-chamber strains
303 were 41.8 and 25.3% respectively. These values were 41.7 and 26.3% for macro-chamber and micro-
304 chamber respectively, under rapid compression. During the hold period while the displacement was
305 kept constant, the load decreased illustrating the stress-relaxation characteristics of the tissue layers.
306 During unloading the heel pad and indenter lost contact around 20% strain. This can be explained by
307 the fact that the heel pad returned to its original shape at a slower rate than the indenter velocity. In
308 viscoelastic modelling, the maximum error was obtained at the middle portion of the loading period
309 where the Ogden material model was not able to simulate the nonlinear behavior of the tissue
310 accurately.

311



312

313 Figure 6. Macro-chamber, micro-chamber and heel pad behaviour under slow and rapid
 314 compression(data used for material properties estimation)

315 **Table 3**

316 Final hyperelastic material properties of the heel pad sub-layers.

317 Values in parenthesis indicate RMS error as a percentage of the maximum force

	μ (MPa)	α (-)	RMS force error (N)	Difference between max strains
Skin	0.452	5.6	1.98 (2.7%) (for the entire heel pad)	-
Micro-chamber	0.095	4.9	3.73 (5.0%)	0.3%
Macro-chamber	0.036	4.5	1.92 (2.6%)	0.4%

318

319 **Table 4**

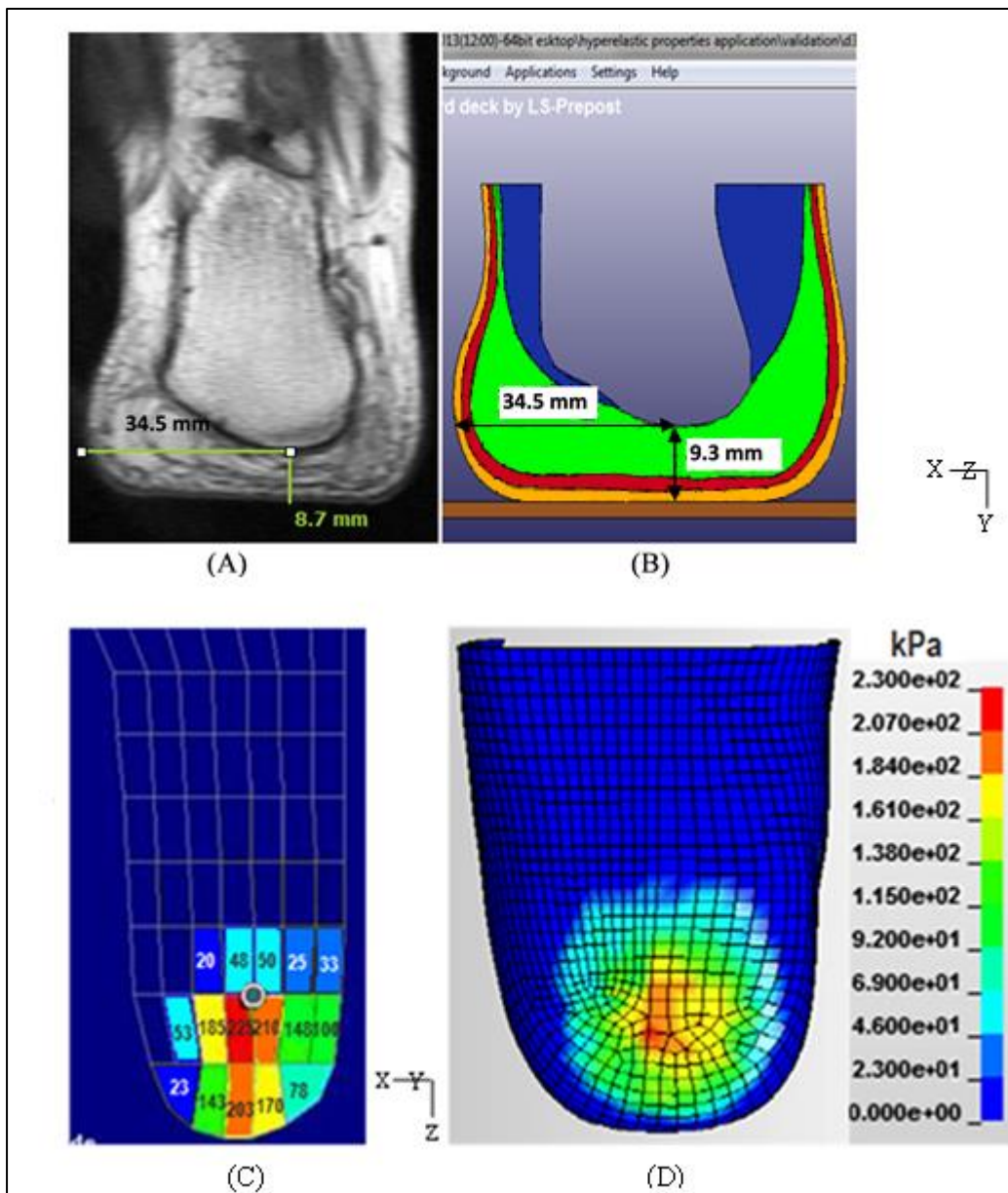
320 Final viscoelastic material properties of the heel pad sub-layers.

321 Values in parenthesis indicate RMS error as a percentage of the maximum force.

	G_1 (MPa)	β_1 (milli-seconds) ⁻¹	RMS force error Loading (N)	RMS force error Unloading (N)
Skin	0.42	0.12	19.88 (17.1%) (for the entire heel pad)	2.15 (1.8%) (for the entire heel pad)
Micro-chamber	0.30	0.12	16.74 (14.4%)	7.44 (6.4%)
Macro-chamber	0.24	0.12	16.91 (14.5%)	3.59 (3.1%)

322

323 The hyperelastic model predicted the loaded (~315N) heel pad thickness within 6.4% of the thickness
 324 measured via MRI. The hyperelastic model showed similar peak plantar pressure compared to the
 325 experimental data from Pedar system. Figure 7 compares the numerical and experimental results of
 326 the plantar pressure under 315N. As shown by the contour plot of the numerical result, the peak
 327 pressure appeared in the central region of the heel with the value 215kPa (averaged over the area of
 328 $10 \times 19 \text{ mm}^2$ that is close to the one sensor size in the Pedar insole). This is comparable with the results
 329 of Pedar system measurements with the value of 225kPa at the very similar location with error of
 330 4.4% maximum peak plantar pressure.



331

332 Figure 7. Validation of hyperelastic model under compressive load of 315N: (A) Loaded MR
333 image of the heel pad; (B) FE model of the loaded heel pad; (C) Pedar pressure insole
334 measurement; (D) FE model pressure prediction

335 The viscoelastic model could simulate the heel pad behaviour with RMS force errors of 13.8-14.7%
336 and 1.6-5.2% of maximum force for loading and unloading periods respectively for rapid loading
337 (141mm/s). The viscoelastic model simulated the heel pad behavior under sinusoidal loading with
338 RMS force errors of 4.5-8.9% and 2.6-5.8% of maximum force for loading and unloading periods
339 respectively.

340 4. Discussion

341 The initial elastic modulus of the macro-chamber, micro-chamber and skin layers was 0.243, 0.698
342 and 3.797MPa, respectively. Direct comparisons to prior literature are difficult because there are no
343 previous reports of the three separate layers. Like our study, Hsu et al. used *in-vivo* data and their
344 elastic modulus of 0.181MPa for the macro-chamber layer concurs quite well with the value reported
345 here (0.243MPa) [29]. Their micro-chamber layer modulus was 1.140MPa, almost twice the stiffness
346 reported here (0.698MPa). This is probably due to Hsu et al. combining the micro and much stiffer
347 skin layers together resulting in an apparent elevation in micro-chamber layer stiffness. Erdemir et al.
348 reported a much lower elastic modulus of 0.050MPa (SD 0.025) for a homogenous heel pad (i.e. all
349 three layers combined) using inverse FEA and *in-vivo* experimental data for 20 subjects [7]. The
350 values obtained here are outside their range and this is perhaps due to their use of an axisymmetric
351 rectangular heel pad model and compression system (a 25.4mm diameter indenter). Using an inverse
352 FEA method, a value of 0.300MPa was reported from impact testing of isolated heel tissue [11],
353 which is comparable with the value for the macro-chamber layer reported here (0.243MPa). In
354 another case, elastic moduli of 0.003 and 6.528MPa were derived for the heel fat pad and skin
355 respectively, based on *in-vitro* and *in-vivo* experimental data [8]. The value for the skin layer of
356 6.528MPa is much higher than the value reported here (3.797MPa), but clearly represents a layer far
357 stiffer than macro and micro layers. The difference is likely due to the small value of 0.003MPa they
358 found for the fat pad based on experimental data from unconfined testing of isolated fat samples.

359 Clearly, different initial elastic moduli have been reported for the heel pad and its sub-layers and data
360 are sensitive to the choice of experimental methods (*in-vivo* or *in-vitro*), age and health of
361 subjects/samples, number of subjects/samples and the degree of simplification of the model used for
362 inverse FEA.

363 Because of variations in material model definitions of α (deviatoric exponent), the values reported
364 here should only be compared to studies which used the same model. In this study α was 4.5, 4.9 and
365 5.6 for the macro-chamber, micro-chamber and skin layers respectively. Erdemir et al. reported a
366 value of 6.82 (SD 1.57) for the entire heel pad [7]. Values of 8.8 and 6.8 have been reported for the fat
367 pad and skin, respectively [8]. It is difficult to judge the appropriateness of direct comparisons since
368 so few participants are used in these experiments and models.

369 A time constant of ~8ms (reciprocal of the decay constant β) was found for all heel pad sub-layers.
370 Values of 1 and 2ms were reported from inverse FEA using compression data of cadaveric intact heel
371 pads [12, 30]. However, they used experimental data collected from a different foot than that used to
372 build the model geometry. In another case, the time constant was 500ms for the heel pad (from
373 experiments on dissected fat pad samples) [13]; a result that may have been affected by dehydration
374 of the sample.

375 The relaxation modulus is represented differently in different FEA software making comparisons
376 difficult. While Ls-Dyna uses shear relaxation modulus (G_1), ABAQUS uses relaxation coefficient (g)
377 which is equal to $G_1/G_\infty+G_1$. G_∞ is the long-term shear modulus and it is $\geq \frac{1}{3}$ of the initial elastic
378 modulus. Based on the above relations, $0 \leq g \leq 1$ and when $g \rightarrow 1$ the material shows characteristics that
379 are more viscoelastic and when $g \rightarrow 0$ the material shows characteristics that are more elastic. Having
380 the initial elastic moduli of the heel pad sub-layers (3.797, 0.698 and 0.243MPa), g was estimated
381 as $\frac{0.42}{(G_\infty \geq 1.26)+0.42} \leq 0.25$, $\frac{0.30}{(G_\infty \geq 0.23)+0.30} \leq 0.57$ and $\frac{0.24}{(G_\infty \geq 0.08)+0.24} \leq 0.75$ for the skin, micro-chamber
382 and macro-chamber respectively. In this study, g complies with the general rule (i.e. is between 0 and
383 1) and from skin to macro-chamber, the viscoelastic behaviour of the materials increases. Previously g
384 was reported as 0.99 using inverse FEA [12, 30], representing a highly viscous heel pad.

385 The 3-layer heel pad model reported here predicted static heel pad thickness under load with an error
386 of 6.4%, which is towards the lower end of the range (5-15%) reported previously for 1-layer and 2-
387 layer models [7, 8, 9, 10]. Spears et al. showed that while a 1-layer model overestimated the plantar
388 heel pressure at the centre of the model (>60% error) and underestimated it at medial and lateral
389 regions (>100% error), a 2-layer model predicted pressures far closer to experimental data (within
390 10%) [8]. Similarly the 3-layer model reported here produced even small error (<4.4% maximum
391 peak plantar pressure); suggesting that the additional increase in model complexity was justified.
392 Unique to this study, the unloading behaviour of the model was evaluated in addition to the behaviour
393 during loading. The errors propagated during the estimation of material properties of the three heel
394 pad sub-layers might be the source of this error. The measurement of the applied load under the heel
395 using Pedar system might be another source of these errors.

396 Since the study included one participant, all findings are unique to the properties of the particular heel
397 studied. It is acknowledged that the inverse FEA process used to determine the material properties,
398 which is based on a manual search procedure, might find different local minima when different initial
399 values for the material properties are used. To simplify the model, identical time constants were used
400 for all three layers. However, given that other properties differ significantly between the layers, this
401 simplification may not be appropriate. All results were obtained for compression loading at a single
402 angle of rotation of the heel and in the absence of shear loading.

403 To our knowledge, this is the first study to estimate the hyperelastic and viscoelastic material
404 properties of the heel pad sub-layers using *in-vivo* data and loading conditions similar to those
405 experienced during gait and standing. Like other FE models, not only can this model predict pressures
406 and shear stresses at the plantar surface but it can also be used to predict internal tissue mechanics.
407 Future work using the model could include studies of the effects of footwear materials on internal
408 stresses and the effects of experimental conditions on heel pad behaviour (such as indenter size and
409 shape).

410 **Conflict of Interest**

411 The authors have no financial or personal relationships with other people or organisations that could
412 inappropriately influence this work.

413 **References**

414

- [1] Hsu CC, Tsai WC, Chen CP, Shau YW, Wang CL, Chen MJ, Chang KJ. Effects of aging on the plantar soft tissue properties under the metatarsal heads at different impact velocities. *Ultrasound in Med and Biol* 2005; 31(10):1423-9.
- [2] Hsu TC, Wang CL, Shau YW, Tang FT, Li KL, Chen CY. Altered heel-pad mechanical properties in type 2 diabetic patients. *Diabetic Med* 2000;17: 854-9.
- [3] Hsu TC, Wang CL, Tsai WC, Kuo JK, Tang FT. Comparison of the mechanical properties of the heel pad between young and elderly adults. *Archives of Phys Med and Rehabilitation* 1998;79(9):1101-4.
- [4] Cavanagh PR, Valiant GA, Misevich KW. Biological aspect of modelling shoe/foot interaction during running. *Fredrick EC, Sport Shoes and Playing Surfaces* 1984;2446.
- [5] Aerts P, De Clercq D. Deformation characteristics of the heel region of the shod foot during a simulated heel strike: the effect of varying midsole hardness. *J Sport Sci* 1993;11:449-61.
- [6] Gefen A, Megido-Ravid M, Itzhak Y. In vivo biomechanical behavior of the human heel pad during the stance phase of gait. *J Biomech* 2001;34: 1661-5.
- [7] Erdemir A, Viveiros ML, Ulbrecht JS, Cavanagh PR. An inverse finite-element model of heel-pad indentation. *J Biomech* 2006;1279-86.
- [8] Spears IR, Miller-Young JE, Sharma J, Smith FW. The potential influence of the heel counter on internal stress during static standing: A combined finite element and positional MRI investigation. *J Biomech* 2007;40:2774-80.
- [9] Gu Y, Li J, Ren X, Lake MJ, Zeng Y. Heel skin stiffness effect on the hind foot biomechanics during heel strike. *Skin Res and Technol* 2010;16: 291-6.
- [10] Chokhandre S, Halloran JP, Bogert AJ, Erdemir A. A three-dimensional inverse finite element analysis of the heel pad. *J Biomech Eng* 2012;134.
- [11] Verdejo R, Mills NJ. Heel-shoe interactions and the durability of EVA foam running-shoe midsoles. *J Biomech* 2004;37:1379-86.
- [12] Spears IR, Miller-Young JE. The effect of heel-pad thickness and loading protocol on measured heel-pad stiffness and a standardized protocol for inter-subject comparability. *Clin Biomech* 2002;21:204-12.
- [13] Miller-Young JE, Duncan NA, Baroud G. Material properties of the human calcaneal fat pad in compression: experiment and theory. *J Biomech* 2002;35:1523-31.

- [14] Ledoux WR, Belvins JJ. The compressive material properties of the plantar soft tissue. *J Biomech* 2007;40:2975-81.
- [15] Bennett MB, Ker RF. The mechanical properties of the human subcalcaneal fat pad in compression. *J Anat* 1990;171:131-8.
- [16] Higa M, Luo Y, Okuyama T, Takagi T, Shiraishi Y, Yambe T. Passive mechanical properties of large intestine under in vivo and in vitro compression. *Med Eng & Phys* 2007;29(8):840-4.
- [17] Ahanchian N, Nester C, Howard D, Ren L. 3D modeling of the human heel pad. Salford Postgraduate Research Conference Proceedings 2012; University of Salford, UK.
- [18] Parker D, Cooper G, Pearson S, Howard D, Crofts G, Nester C. In vivo measurements of the biomechanical properties of plantar soft tissues under simulated gait conditions. *J Foot and Ankle Res* 2012;5.
- [19] Cheung JTM, Zhang M, Leung AKL, Fan YB. Three-dimensional finite element analysis of the foot during standing—a material sensitivity study. *J Biomech* 2005;38(5):1045-54.
- [20] Antunes PJ, Dias GR, Coelho AT, Pereira T. Nonlinear 3D foot FEA modelling from CT scan medical images. *Comput Vision and Med Imaging Process* 2008;135-41.
- [21] Gefen A, Megido-Ravid M, Itzchak Y, Arcan M. Biomechanical evaluation of surgical plantar fascia release effects. *J. Willard Marriott Digital Library, University of UTAH*, 2014.
- [22] Wu L. Nonlinear finite element analysis for musculoskeletal biomechanics of medial and lateral plantar longitudinal arch of Virtual Chinese Human after plantar ligamentous structure failures. *Clin Biomech* 2007;22(2):221–9.
- [23] Cheung JTM, Zhang M. An effect of plantar fascia stiffness on the biomechanical responses of the ankle-foot complex. *Clin Biomech* 2004;19(8):839-46.
- [24] Wright D, Rennels D. A study of the elastic properties of plantar fascia. *J Bone and Joint Surgery* 1964;46(3):482-92.
- [25] Kitaoka H. Material properties of the plantar aponeurosis. *Foot & Ankle Int* 1994;15(10):557-60.
- [26] Untaroiu C, Shin J, Crandall J. Development and validation of a headform impactor finite element model with application to vehicle hood design for pedestrian protection. *LS-DYNA Conference Proceedings 2006; Dearborn, Michigan, USA*.
- [27] Kinoshita H, Oqawa T, Kuzuhara K, Ikuta K. In-vivo examination of the dynamic properties of the human heel pad. *J Sport Med* 1993;14(6):312-9.
- [28] Hajjarian Z, Nakarni SK. Evaluating the viscoelastic properties of tissue from laser speckle fluctuations. *Scientific Reports* 2012; 2(316).
- [29] Hsu CC, Tsai WC, Hsiao TY, Tseng FU, Shau YW, Wang CL, Lin SC. Diabetic effects on microchambers and macrochambers tissue properties in human heel pads. *Clin Biomech*

2009;24:682-86.

[30] Spears IR, Miller-Young JE, Waters M, Rome K. The effect of loading conditions on stress in the barefooted heel pad. *Med and Sci in Sports and Exercise* 2005;1030-6.

415

416